Available online at www.sciencedirect.com

ScienceDirect

Geochimica et Cosmochimica Acta 312 (2021) 343–356

Geochimica et Cosmochimica Acta

www.elsevier.com/locate/gca

Photocatalytic oxidation of dissolved Mn(II) on natural iron oxide minerals

Haesung Jung [a,b,1], Xiaoming Xu [a,c,1], Biao Wan [a], Qian Wang [a], Olaf J. Borkiewicz [d], Yan Li [c], Hailong Chen [e], Anhuai Lu [c,*], Yuanzhi Tang [a,*]

[a] School of Earth and Atmospheric Sciences, Georgia Institute of Technology, Atlanta, GA 30332-0340, United States
[b] School of Civil, Environmental and Chemical Engineering, Changwon National University, Changwon, Gyeongsangnam-do 51140, Republic of Korea
[c] Beijing Key Laboratory of Mineral Environmental Function, School of Earth and Space Sciences, Peking University, Beijing, China
[d] Advanced Photon Source, Argonne National Laboratory, Argonne, IL 60439, United States
[e] School of Mechanical Engineering, Georgia Institute of Technology, Atlanta, GA 30332, United States

Received 20 January 2021; accepted in revised form 20 July 2021; available online 28 July 2021

Abstract

The energy conversion in Earth's surface environments over geological history heavily involves the redox reactions of natural minerals. Natural Mn(III/IV) oxides and Mn^{2+}(aq) is one of the most important redox couples that significantly dictate the electron flow in nature. Elucidating their formation and redox reactions is of critical importance for understanding numerous elemental cycles and the evolution of redox environments on Earth and other planets. Previous studies generally consider biotic processes as the dominant oxidation pathway for Mn^{2+}(aq) in natural environments. In this study, we demonstrate rapid abiotic oxidation of Mn^{2+}(aq) through photocatalytic reactions in the presence of natural Fe oxide minerals at rates comparable to those of currently known biotic/abiotic oxidation processes. Fe oxide minerals not only facilitate the electron transfer, but also serve as templates for the heterogeneous nucleation of tunnel structured Mn oxides. This finding highlights an important yet previously overlooked abiotic process on the formation of Mn oxides, which offers a new pathway for explaining the commonly observed co-occurrence of Fe and Mn oxide minerals in nature and the origin of diverse structures of Mn oxides.

Keywords: Mn oxide; Photochemistry; Fe oxide; Tunnel structure

1. INTRODUCTION

Mn(III, IV) (oxyhydr)oxides (hereafter noted as Mn oxides) are a group of metal oxides of great environmental, geological, and public health significances. They exist in nearly all environmental settings, such as aquatic systems, soils, and sediments, and significantly influence the biogeochemical cycling of numerous metals, nutrients, and organic compounds through adsorption, precipitation, and redox reactions. They are among the strongest natural oxidants and can participate in a wide range of redox reactions involving organic and inorganic species (e.g., Stone and Morgan, 1984; Fendorf and Zasoski, 1992; Sunda and Kieber, 1994; Murray et al., 2007). In the absence of oxygen, Mn oxides can be used by dissimilatory metal-reducing bacteria as the terminal electron acceptor for the oxidation of organic matter (Nealson and Saffarini, 1994), thus further affecting the carbon cycle. Moreover, due to

* Corresponding authors.
E-mail addresses: ahlu@pku.edu.cn (A. Lu), yuanzhi.tang@eas.gatech.edu (Y. Tang).
[1] The authors contributed equally.

https://doi.org/10.1016/j.gca.2021.07.023
0016-7037/

the high reduction potential of Mn, the widespread occurrence of Mn oxides was suggested to be indicative of highly oxidizing aqueous environment, providing clues for the early evolution of redox environments on Earth and Mars (Lanza et al., 2014). For example, the Mn redox cycle is built into the fundamental frameworks of several newly proposed paleo redox proxy systems for tracking Earth's oxygen evolution history, such as the Ce, Mo, Cr, and Tl isotope systems (Frei et al., 2009; Crowe et al., 2013; Planavsky et al., 2014b; Owens et al., 2017; Goto et al., 2020), as Mn oxides play critical roles in the redox cycles of these elements and related isotope fractionations. Thus, understanding Mn oxide formation can greatly advance our knowledge of the operation and evolution of planetary surface environments.

The formation of Mn oxides originates from the oxidation of Mn(II) or soluble Mn(III) complexes. Although the oxidation of Mn^{2+}(aq) by molecular oxygen via one-electron transfer is thermodynamically favorable at pH higher than ~8 (Luther III, 2010), abiotic homogeneous oxidation of Mn^{2+}(aq) in aqueous condition takes years (Diem and Stumm, 1984). With the common presence of Mn oxide coatings on the surface of natural minerals, heterogeneous oxidation of Mn^{2+}(aq) by molecular oxygen on mineral surfaces has been considered as a possible abiotic pathway for Mn oxide formation. Studies of heterogeneous oxidation of Mn^{2+}(aq) on the surface of Fe/Al oxides and silica showed that mineral surface-catalyzed heterogeneous oxidation of Mn^{2+}(aq), with a half-life of 5–2,800 days, is faster than homogeneous oxidation of Mn^{2+}(aq) in solution by molecular oxygen (Sung and Morgan, 1981; Davies and Morgan, 1989; Wehrli et al., 1995). However, except for the study on the heterogeneous nucleation of Mn(III) oxide by ~7 nm hematite nanoparticles (Table S1) (Madden and Hochella, 2005), the rates of these heterogeneous oxidation reactions are much lower than those observed in nature (a half-life of ~1.4 days) (Wehrli et al., 1995). In addition, while Mn(IV) is the most dominant oxidation state of natural Mn oxides, only Mn(III) oxides were observed in previous laboratory studies of heterogeneous oxidation processes (Sung and Morgan, 1981; Davies and Morgan, 1989; Wehrli et al., 1995). In contrast, compared to the slow abiotic processes, microbially mediated processes show much faster oxidation of Mn^{2+}(aq) to Mn (IV) within hours (Webb et al., 2005b; Hansel et al., 2012; Butterfield et al., 2013). Thus, based on the ubiquitous presence of Mn(II)-oxidizing microorganisms, biotic processes are generally considered to be the dominant contributor to the formation of natural Mn oxides in surficial systems.

A few earlier studies showed that mineral-catalyzed or photochemical processes might also contribute significantly to the oxidation of Mn^{2+}(aq) in environmental systems. Madden and Hochella showed 1–1.5 orders of magnitude higher rate of heterogeneous oxidation of Mn^{2+}(aq) on ~7 nm hematite nanoparticles as compared to that of ~37 nm hematite nanoparticles (Table S1) (Madden and Hochella, 2005). Anbar and Holland showed rapid anoxic oxidation of Mn^{2+}(aq) by UV light (180–240 nm) (Anbar and Holland, 1992), which became insignificant upon the addition of Fe^{2+}(aq). Following these seminal studies on mineral/photochemistry assisted oxidation of Mn^{2+}(aq), several recent studies have sparkled interests in the re-assessment of light-induced biotic/abiotic processes in the oxidation of Mn(II) and formation of Mn oxides. For example, studies showed the oxidation of Mn^{2+}(aq) by phototrophic organisms (Learman et al., 2011a; Chaput et al., 2019; Daye et al., 2019). In abiotic processes, reactive oxygen species (such as superoxide) generated from the photochemical reduction of oxygen in the presence of organics or nitrate (i.e., an indirect photochemical oxidation process) are reported to show considerable Mn^{2+}(aq) oxidation (Nico et al., 2002; Learman et al., 2011b; Jung et al., 2017a). These studies used high concentrations of organic matter (5 mg/L) (Nico et al., 2002) or nitrate (14 mg/L) (Jung et al., 2017a) as compared to their typical concentrations in surface waters (~0.5 mg/L organic matter and ~0.7 mg/L nitrate (Millero, 2016)). Considering the wide range of dissolved organic matter (~0.1 to ~50 mg/L) and nitrate concentrations (0 to ~20 mg/L) in surface waters (Mulholland, 1997; World Health, 2003), such abiotic photochemical oxidation of Mn^{2+}(aq) might be significant in certain environmental settings.

Based on the known high photocatalytic performance of Fe oxide minerals in engineering systems and considering the widespread co-existence of Fe and Mn oxides in nature, we are inspired to systematically explore the possibility of natural Fe oxide minerals assisted direct photocatalytic oxidation of Mn^{2+}(aq) in sun-lit environments, as well as the roles of Fe oxides in the formation of different structured Mn oxides. A recent study demonstrated that the photon-to-electron conversion by semi-conducting Fe oxides on rock surfaces is possible (Lu et al., 2019). The ubiquitous occurrence of Mn/Fe oxide enriched rock varnishes on sun-lit rock surfaces strongly suggests the possibility of photocatalytically induced formation of Mn oxides in the presence of Fe oxides (Lu et al., 2019). A recent study reported the photochemical oxidation of Mn^{2+}(aq) on natural Fe oxides and TiO_2, and the authors proposed an indirect pathway of Mn^{2+}(aq) oxidation by reactive oxygen species (ROS) generated through the transfer of photo-excited electron to dissolved oxygen in solutions (Xu et al., 2019). We hypothesize that, in the presence of light and minerals, direct photocatalytic oxidation of Mn^{2+}(aq) (i.e., electron transfer from Mn^{2+}(aq) to the valence band of natural minerals) is a possible reaction pathway, and the rate of oxidation relies on the photocatalytic reactivity of the mineral substrate and solution chemistry. We further hypothesize that the mineral particles might serve as an underlying template to lower the formation energy and facilitate the heterogeneous nucleation of Mn oxides, and the phase of Mn oxides might be influenced by the mineral substrate structure and surface properties.

On the other hand, previously studied biotic or abiotic homogeneous oxidation processes typically induced the precipitation of highly disordered nanocrystalline layered Mn oxides that are structurally similar to vernadite (δ-MnO_2) or hexagonal birnessite (Learman et al., 2011b; Jung et al., 2017b). This phase is highly reactive and can subsequently undergo abiotic transformations or ripening to form more ordered and crystalline phases such as

triclinic birnessite, feitknechtite, and todorokite (Bargar et al., 2005; Feng et al., 2010; Elzinga, 2011; Learman et al., 2011b). As the other dominant structure category of Mn oxides, tunnel structured Mn oxides are also commonly observed in nature (Potter and Rossman, 1979; Post, 1999). Yet their formation and occurrence are still not fully understood. One study reported the direct microbial precipitation of tunnel structured Mn oxides such as todorokite (Santelli et al., 2011) but with no detailed reaction mechanism proposed. To our knowledge, no previous studies have reported the direct formation of tunnel structured Mn oxides through abiotic processes under conditions similar to low temperature circumneutral environments (Feng et al., 2004, 2010; Yang et al., 2018, 2021).

In this study, we designed systematic laboratory experiments to explore the photochemical oxidation of Mn^{2+} in the presence of natural Fe oxide minerals (hematite and goethite) under simulated freshwater and seawater conditions. We found that the photocatalytic oxidation of Mn^{2+}(aq) by these Fe oxides under circumneutral pH conditions is not only viable, but comparable to previously reported biotic/abiotic processes. This exciting finding suggests that such mineral-catalyzed photochemical oxidation of Mn^{2+}(aq) may serve as an important yet previously overlooked pathway for Mn oxide formation. We also found that large tunnel structured Mn (III/IV) oxides can occur through heterogeneous nucleation on Fe oxides and in the presence of large cations in circumneutral conditions. Considering the ubiquitous presence of Fe oxides in nature, our findings provide a new perspective for understanding the occurrence and diversity of Mn oxide phases in sun-lit natural environments.

2. METHODS

2.1. Materials and reagents

Three environmentally abundant Fe oxide minerals (ferrihydrite, goethite, and hematite) were synthesized following previous procedures (Cornell and Schwertmann, 2003). After synthesis, the solids were repeatedly washed by deionized (DI) water, dialyzed, and freeze dried. X-ray diffraction (XRD) analysis confirmed the synthesized minerals to be phase pure (Fig. S1). Surface area of the minerals was analyzed using the Brunauer–Emmett–Teller (BET) method with N_2 gas adsorption (Autosorb-1-MP surface pore analyzer, Quantachrome Corp.), and the measured specific surface areas are 236.11 ± 1.49, 38.44 ± 0.39, and 117.96 ± 0.43 $m^2\ g^{-1}$ for ferrihydrite, goethite, and hematite, respectively.

To simulate natural freshwater and seawater conditions, photochemical experiments were conducted in both DI and artificial seawater (ASW). ASW contained 0.42 M NaCl, 0.025 M $MgSO_4$, 0.0091 M $CaCl_2$, 0.0089 M KCl, and 0.0024 M $NaHCO_3$, with an initial pH of 8 (Montserrat et al., 2017). During the 8 h experimental course, pH of the ASW stayed at 7.95 ± 0.05. The pH of the DI water was initially titrated to 7.5 using HCl and NaOH. Throughout the reaction, the pH value of the DI water dropped by ~0.3 unit per hour, and was manually adjusted to 7.5 ± 0.1 using 0.1 M NaOH every hour.

Prior to the start of experiments, Fe oxides (0.1 g/L) were suspended in 180 mL DI or ASW, followed by dispersion via sonication. The sizes of the Fe oxide particles suspended in DI and ASW were measured before light exposure using dynamic light scattering (Zetasizer). We used z-average (intensity-weighted mean hydrodynamic sizes) mean value because it is sensitive to the size of aggregated particles. Calculated aliquots of $MnCl_2$ stock solution were added to the suspension to achieve 100 μM final concentrations.

2.2. Photocatalytic oxidation of Mn^{2+}(aq)

Photochemical reactions were initiated by exposing the above-prepared suspension to a 450 W Xe-arc lamp light source (Newport) equipped with a 10 cm IR water filter (to avoid temperature increase during reaction). A gas-tight borosilicate reactor with a quartz window (1 in. diameter) was used for the reaction. The reaction suspension was continuously stirred on a magnetic stir plate during the reactions. Aliquots (0.3 mL) of the suspension were periodically sampled for solid and aqueous phase analyses. All experiments were conducted in replicate.

To calculate quantum yields and to estimate oxidation rates under natural sunlight conditions, we used the irradiances of 450 W Xe-arc lamp and reference solar spectral irradiance from the National Renewable Energy Laboratory (NREL) website. A set of parallel experiments were also conducted using 400, 550, and 645 nm cut-off optical filters (Newport) to identify the photo-active wavelength range for Mn^{2+}(aq) oxidation.

Two sets of control experiments were conducted to evaluate the effects of light and oxygen exposure. Dark experiments were conducted without the light source. Anoxic experiments were conducted by purging all the reaction solutions with ultrahigh purity N_2 gas. The purged solutions were transferred into a controlled atmosphere glove box (95%:5% N_2/H_2) (Coy), inside which the reaction suspension was transferred into the gas-tight borosilicate reactor. Photochemical reaction was conducted outside the glove box. At each sampling point (typically every hour), the reactor was transferred into the glove box for aliquot sampling.

To test the potential formation and effect of reactive oxygen species (ROS) on the oxidation of Mn^{2+}(aq), a set of parallel experiments were also conducted in the presence of 0.1 μM superoxide scavenger, superoxide dismutase (SOD, ≥2500 units/mg protein, Sigma Aldrich), or 0.1 M hydroxyl radical scavenger, t-BuOH (Sigma Aldrich). We chose 0.1 μM SOD for scavenging superoxide based on the results from nitrate-catalyzed photochemical oxidation of Mn^{2+}(aq), which showed clear suppression of photochemical oxidation in the presence of SOD (Jung et al., 2017a). In addition, as a positive control to produce superoxide and confirm the scavenging performance of 0.1 μM SOD, we tested the photocatalytic oxidation of Mn^{2+}(aq) by TiO_2 nanoparticles, which have a large enough band-

gap to produce superoxide via photocatalysis. Under the same conditions of Fe oxides, our tests for the photocatalysis by TiO_2 in the presence of SOD showed a clear difference on the photocatalytic oxidation of Mn^{2+}(aq) by TiO_2 (date not shown), indicating that the use of 0.1 μM SOD is sufficient to confirm the contribution of superoxide in the photocatalytic oxidation of Mn^{2+}(aq) by Fe oxides. t-BuOH is the most representative scavenger of hydroxyl radical (Wu et al., 2018). The addition of the high concentration (0.1 M) of t-BuOH ensures the quenching of the oxidation of Mn^{2+}(aq) by hydroxyl radical.

2.3. Characterization of reaction products

At each time point, aliquots of the reaction suspension were sampled. The amount of oxidized Mn(III,IV) was quantified for both unfiltered and syringe filtered (0.2 μm) suspension using the leucoberbelin blue (LBB) colorimetric method (Tebo et al., 2007) at 625 nm on an UV–vis spectrophotometer (Cary 60, Agilent). Standard calibration used $KMn^{VII}O_4$. LBB has one electron transfer with Mn species with an oxidation state higher than Mn(II). That is, one mole of Mn(VII) oxidizes five moles of LBB. Thus, the oxidizing equivalent can be converted to different Mn valences. For example, 10 μM $KMn^{VII}O_4$ (oxidizing 50 μM LBB) is equivalent to 50 μM of $Mn^{III}OOH$ (oxidizing 50 μM LBB). Due to the difference in crystal structure and oxidation state of the produced Mn oxides, Mn(III, IV) concentration measured by the LBB method was converted to Mn(III) equivalent to enable cross comparison among different experiments. Because the solutions in DI and ASW systems do not contain ligands for stabilizing soluble Mn(III), dissolved Mn^{2+} concentration was directly determined using the porphyrin colorimetric method at 468 nm on a UV–vis spectrophotometer (Madison et al., 2011).

At the end of reactions, solid products were collected through vacuum filtration (0.2 μm), followed by repeated DI rinse and freeze drying. Freeze dried solids were finely ground and characterized for structure properties using X-ray photoelectron spectroscopy (XPS), X-ray diffraction (XRD), and X-ray absorption spectroscopy (XAS). Synchrotron XRD was conducted at Beamline 11-ID-B ($E = 58.648$ keV, $\lambda = 0.2114$ Å) at the Advanced Photon Source (APS) at Argonne National Laboratory (Lemont, IL, US). XPS analysis was conducted on a K-alpha XPS system (ThermoFisher Scientific). C 1s spectra (284.8 eV) were used for the calibration of binding energy. Mn 3p spectra were used for spectra fitting and obtaining Mn oxidation state because it shows better sensitivity than Mn 2p and 3s spectra. For the fitting of Mn 3p spectra, FWHM was limited in the range of 1.5–1.9 based on the fitting of reference Mn oxides ($Mn^{II}O$, γ-$Mn^{III}OOH$, and β-$Mn^{IV}O_2$) (Fig. S2). In addition, as shown in a previous study for the curve fitting of Mn 3p spectra (Cerrato et al., 2011), asymmetrical Gaussian-Lorentzian algorithm was applied by giving a freedom on the tail mix in the Mn 3p spectra fitting above 80%.

Synchrotron Mn K-edge X-ray absorption spectroscopy (XAS) analysis was conducted at Beamline 4-1 at the Stanford Synchrotron Radiation Lightsource (SSRL, Menlo Park, CA, US), Beamline 5-BM-D at APS, and Beamline 6-BM at National Synchrotron Light Source-II (NSLS-II) at Brookhaven National Laboratory (Upton, NY, US). Solids were brushed on Kapton tapes and XAS data was collected in both transmission and fluorescence mode. Both XANES (X-ray absorption near edge structure) and EXAFS (extended X-ray absorption fine structure) data were collected. The monochromators were detuned by 40% to avoid higher order harmonics. Energy calibration used Mn foil. Multiple scans (2–6) were collected for each sample, averaged, and normalized for further analysis. Analysis of the Mn XANES spectra for each sample showed no evidence of photo-reduction under the X-ray beam.

XAS data analysis was performed using the programs SIXPACK (Webb, 2005) and Ifeffit (Ravel and Newville, 2005). Linear combination fitting (LCF) of the Mn XANES region was conducted to determine the relative percentage of Mn(II), Mn(III), and Mn(IV) species and the average oxidation state (AOS) following previous procedures (Manceau et al., 2012). To obtain statistically meaningful fitting results, all possible combinations with up to four reference compounds among the 12 reference compounds in Table S2 were applied, and 781 different fitting results were obtained. Note that each reference compound only contains one oxidation state of Mn(II), Mn(III), or Mn(IV), whereas the Mn oxides produced in this study likely contain multiple oxidation states. Among the obtained fitting results, 30 fittings with the lowest R factors were averaged to determine AOS and the relative percentages of different Mn oxidation states. Typical error for LCF is ~10% based on the 30 fitting results. Thus, values lower than 5% are considered negligible. Details on the reference compounds and results for LCF analysis are in Table S2. LCF for EXAFS spectra is also conducted to analyze the structure of the heterogeneously nucleated Mn oxides on Fe oxides. EXAFS spectra of references compounds for LCF are available in the Supplementary Information (Fig. S3).

3. RESULTS

3.1. Light and Fe oxide facilitated oxidation of Mn^{2+}(aq)

Our systematic experiments investigated the photochemical oxidation of Mn^{2+}(aq) in the combined presence of light and natural Fe oxide minerals hematite or goethite. With 8 h light exposure, both hematite and goethite oxidized Mn^{2+}(aq) and led to the production of >80 and >60 μM Mn(III) equivalent, respectively. Here the Mn (III,IV) concentrations measured by the leucoberbelin blue (LBB) method were converted to Mn(III) equivalent to enable direct comparison between different experiments (Fig. 1). Note that the oxidation rate calculation (Fig. S4) is also based on Mn(III) equivalent. Interestingly, minimal to negligible oxidation occurred in the presence of ferrihydrite. The rate and extent of oxidation were also affected by solution chemistry, as evidenced by the differences in DI water vs ASW (representing freshwater and marine conditions, respectively). For hematite system, in both

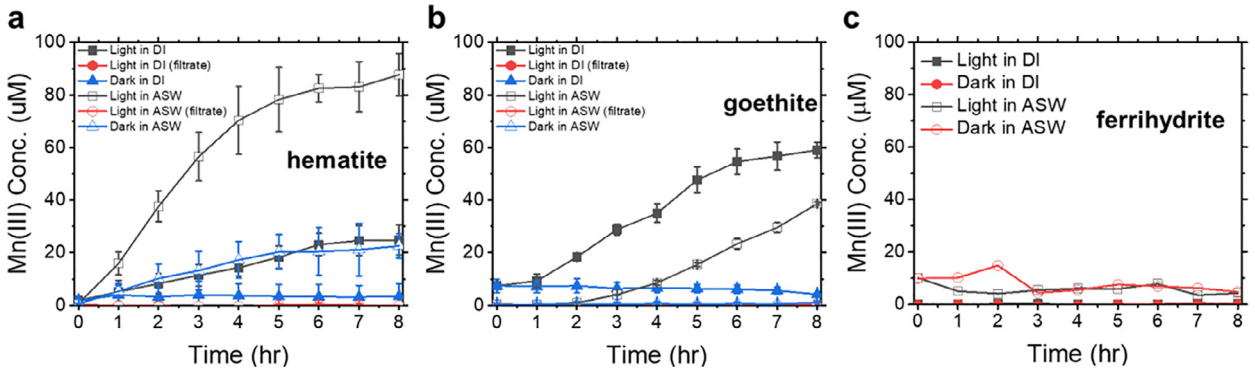

Fig. 1. The photocatalytic oxidation of Mn^{2+}(aq) in the presence of hematite (a), goethite (b), and ferrihydrite (c) in DI water and ASW. For the photocatalytic oxidation of Mn^{2+}(aq) in the presence of hematite (a), the difference between filtered and non-filtered samples suggests the formed Mn oxides are present as solid phases. As explained in the Method section, Mn(III,IV) concentration measured by LBB method was converted to Mn(III) equivalent to enable cross comparison among different experiments.

DI-hematite and ASW-hematite suspensions, rapid oxidation occurred within the first 6 h, followed by a plateau. The oxidation of Mn^{2+}(aq) (calculated using initial linear range) in ASW-hematite suspension (18.7 ± 3.1 μM h^{-1}) was six times faster than that in DI-hematite suspension (3.2 ± 1.4 μM h^{-1}) (Fig. 1a and Fig. S4). In ASW-hematite suspension, the extent of oxidation appears to be limited by the consumption of Mn^{2+}(aq) (Fig. S5). For goethite system, in contrast, higher oxidation extent was observed in DI-goethite suspension than ASW-goethite suspension (Fig. 1b). Oxidation in ASW-goethite suspension also exhibited a ~3 h delay as compared to the immediate onset in DI-goethite suspension. After 3 h, the oxidation rate in DI-goethite suspension (8.6 ± 0.7 μM h^{-1}) was only slightly higher than in ASW-goethite suspension (6.5 ± 0.7 μM h^{-1}) (Fig. S4).

Dark control experiments in the presence of hematite and goethite showed no significant oxidation of Mn^{2+}(aq), suggesting that photochemical reaction was the dominant (if not only) factor for the induction of fast oxidation, except for the dark control experiment of ASW-hematite. It is worth noting that the hematite system (Fig. 1a) showed considerable oxidation under dark ASW condition (~20 μM Mn(III) production at steady state), although no oxidation occurred under dark DI condition (Fig. 1a). This is possibly due to mineral catalyzed heterogeneous oxidation as previously observed on hematite surface (Table S1) (Madden and Hochella, 2005). The dark control experiments showed significant effects of light on the oxidation of Mn^{2+}(aq) by Fe oxides.

Control experiments using scavengers for superoxide or hydroxyl radical, both being the most common and reactive ROS species in nature, show that the photocatalytic oxidation of Mn^{2+}(aq) by Fe oxides occur at similar rates (Fig. 3a and b), although there is a slight difference in the oxidation extents.

Anoxic test explored the effect of oxygen on the photocatalytic oxidation of Mn^{2+}(aq). Under anoxic conditions, both hematite and goethite showed no discernible oxidation of Mn^{2+}(aq), indicating the necessity of oxygen for the rapid photocatalytic oxidation by Fe oxides (Fig. 3d and e). To reveal the effective wavelength region of photocatalysis, we conducted parallel experiments for the ASW-hematite system using 400, 550, and 645 nm cut-off optical filters, which can block lights below 400, 550, or 645 nm, respectively. A considerable decrease in Mn^{2+}(aq) oxidation (from ~80 to ~60 μM at steady state) was observed only for the 645 nm filter (Fig. 3g), suggesting that electron transfer between hematite and Mn^{2+}(aq) occurs dominantly at ~650 nm (~1.9 eV).

3.2. Heterogeneous nucleation and formation of Mn oxides

In addition to the observed fast photocatalytic oxidation of Mn^{2+}(aq) in the presence of hematite/goethite, we also observed the heterogeneous nucleation and formation of tunnel structured Mn(III/IV) oxides on the surface of Fe oxides as reaction products. Homogeneous nucleation typically results in nanometer-sized particles in solution (De Yoreo et al., 2015), which would have penetrated the 0.2 μm syringe filters at least during the early stages of reaction. Previous study of homogeneously nucleated Mn oxides in biotic and abiotic processes showed that the size of the Mn oxide nuclei is in the range between ~6 and ~30 nm (Soldatova et al., 2019). However, no Mn(III/IV) solids were detected in the filtrate at any time during the reaction (Fig. 1a and b), confirming the heterogeneous nucleation of Mn oxides on Fe oxide surfaces.

Mn 3p X-ray photoelectron spectroscopy (XPS) analysis of the filtered final solids revealed that Mn(III) was the most dominant oxidation state (92%, 66%, 51%, and 39% for DI-goethite, ASW-goethite, DI-hematite, and ASW-hematite suspensions, respectively), followed by Mn(IV) (26–29%) and Mn(II) (8–35%) (Fig. S6). Notably, DI-goethite suspension produced oxidized Mn almost exclusively as Mn(III) (92%, with the remaining 8% as Mn(II)). The presence of Mn(II) in the solid products is likely due to its adsorption on the Fe oxide and/or precipitated Mn oxide surfaces. Linear combination fitting (LCF) of Mn K-edge XANES data showed similar trends as XPS-obtained fractions of Mn(III) and Mn(IV) species (Table S3). Although both techniques provided qualitative

trends with respect to the oxidation states of Mn(III/IV) species produced, as shown in the different trend in DI-hematite and ASW-hematite suspensions, obtaining accurate ratios of Mn(III)/Mn(IV) was difficult due to errors associated with data fitting and the difference between bulk technique (XANES) and near-surface technique (XPS) (Ilton et al., 2016).

Reactions in hematite suspension also induced the formation of romanechite-like Mn oxide phase (2 × 3 tunnel structure) (Fig. 2a). Strong XRD peaks at ~3.4 and ~2.4 Å were observed for Mn oxides precipitated in ASW-hematite suspension. Among all known Mn(III/IV) oxide phases, these peaks only belong to romanechite. The observed diffraction peaks are slightly shifted from the reference compound Ba-romanechite, possibly due to the presence of other cations such as Ca^{2+}, Mg^{2+}, and Na^{+} (from ASW) instead of Ba^{2+} in the tunnels. For reaction products from the DI-hematite suspension, fewer and weaker diffraction peaks were observed as compared to the solids from ASW-hematite suspension, making accurate phase identification difficult. However, LCF of EXAFS spectra at 7–10 $Å^{-1}$ k-space (the well-known "indicator region" for layer and tunnel structured Mn oxides (Fig. S7) (McKeown and Post, 2001; Webb et al., 2005a; Saratovsky et al., 2009; Santelli et al., 2011)) also suggests the formation of romanechite-like phase (Webb et al., 2006), likely with other cations in the tunnels.

Photocatalytic reaction in DI-goethite suspension induced the formation of groutite (α-MnOOH), a 1 × 2 tunnel structured Mn oxide phase (Fig. 2b). XRD showed the appearance of groutite (301) and (401) diffraction peaks, consistent with Mn XANES and EXAFS analyses (Fig. 2c and Fig. S7 and S8). Since goethite (α-FeOOH) is an α-MeOOH phase with a 1 × 2 tunnel structure, the matching lattice structure with groutite suggests a likelihood of templated nucleation and growth of groutite on

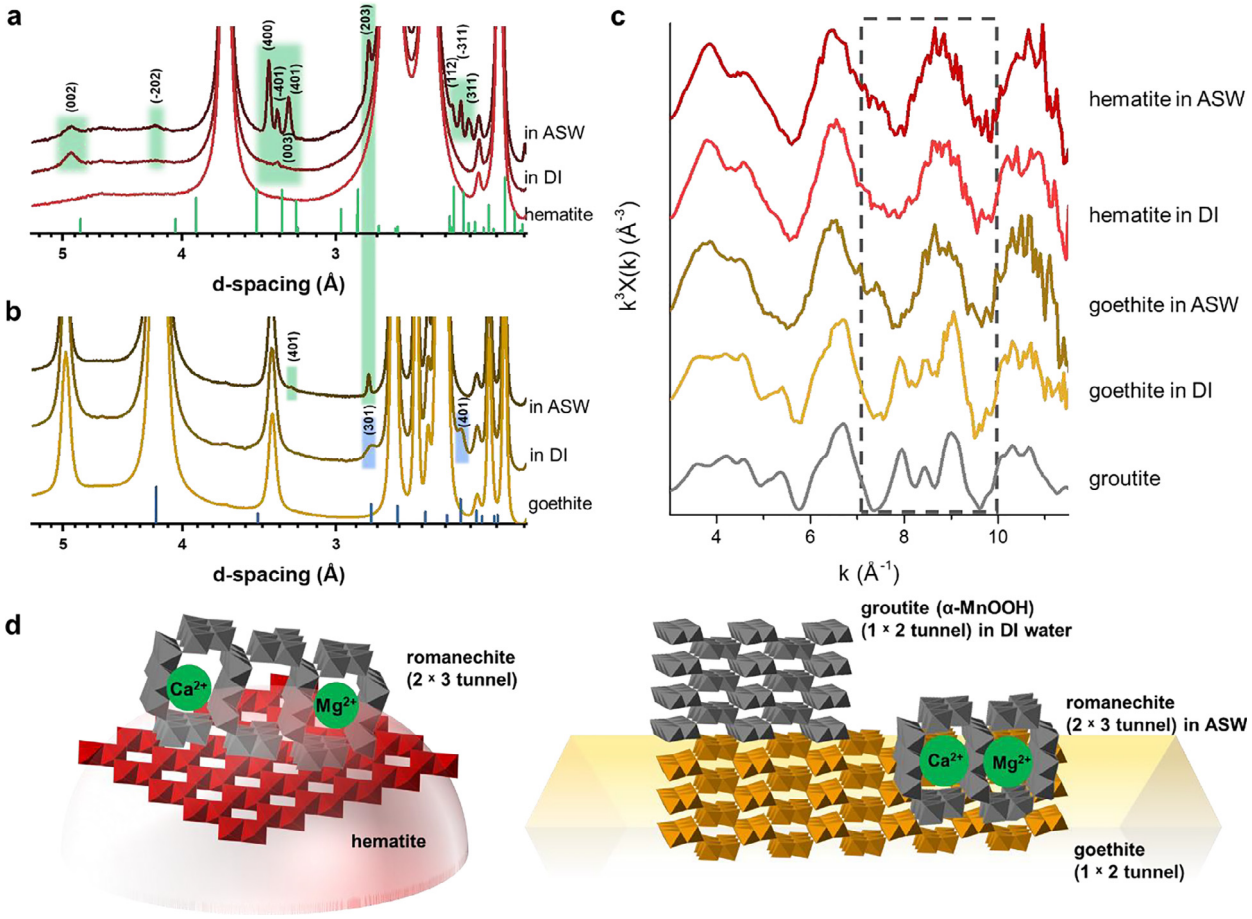

Fig. 2. Heterogeneous nucleation of Mn(III/IV) oxides on hematite and goethite surfaces. (a) XRD data showing the formation of romanechite-like Mn oxide (2 × 3 tunnel structure) phase on hematite. Bottom green vertical lines indicate the diffraction peak positions of Ba-romanechite reference, with green vertical bars indicating the (h k l) of the observed diffraction peaks of romanechite in reacted samples. (b) XRD data showing the formation of groutite-like Mn oxide phase (1 × 2 tunnel structure) on goethite in DI. Bottom blue vertical lines indicate the diffractions of groutite reference, with blue vertical bars indicating the (h k l) of the observed diffractions of groutite in the reacted samples. (c) Mn K-edge EXAFS results supporting the formation of groutite on goethite. EXAFS data in the 7–10 $Å^{-1}$ indicator region (highlighted by dashed lines) of hematite in ASW, hematite in DI water, and goethite in ASW indicate the formation of romanechite. (d) Schematic illustration of heterogeneously nucleated Mn oxides on hematite and goethite surfaces through photocatalytic oxidation. (For interpretation of the references to colour in this figure legend, the reader is referred to the web version of this article.)

goethite. For ASW-goethite suspension, weak XRD peaks for both groutite and romanechite were observed, though EXAFS spectra suggested the dominance of a romanechite-like structure.

4. DISCUSSION

4.1. Mechanisms for Fe oxide catalyzed photocatalytic oxidation of Mn^{2+}(aq)

As discussed previously, we consider direct photocatalysis as the dominant (if not only) factor for light and Fe oxide facilitated Mn^{2+}(aq) oxidation. Superoxide and hydroxyl radical have been considered as the most effective oxidizer in photochemical reactions due to their high reactivity and environmental abundance. Recent studies have reported the indirect oxidation of Mn^{2+}(aq) by photochemically generated superoxide (Learman et al., 2011a; Jung et al., 2017a)) in solution (i.e. homogenous oxidation). However, in our study, the conduction bands of hematite and goethite are at higher potential than the reduction potential of oxygen/superoxide (Fig. 3c) (Xu and Schoonen, 2000; Wu et al., 2015). Therefore, photo-excited electrons of goethite and hematite cannot reduce dissolved oxygen to superoxide. Previous studies also showed that hydroxyl radical is not an effective oxidant of Mn^{2+}(aq) under neutral pH condition (Learman et al., 2011a; Jung et al., 2017a) even though this process is thermodynamically feasible (Luther III, 2010; van Genuchten and Peña, 2017). Our control experiments using the scavengers superoxide dismutase (SOD; targeting superoxide) and t-BuOH (targeting hydroxyl radical) showed similar Mn^{2+}(aq) oxidation rates as compared to the experiments without scavengers (Fig. 3a and b), suggesting negligible contributions of superoxide and hydroxyl radical on the observed oxidation of Mn^{2+}(aq). The effect of singlet oxygen and H_2O_2 on the oxidation of Mn^{2+}(aq) is ruled out because they are not likely produced via the photocatalysis of Fe oxides. However, since the chemistry of ROS is quite complicated, future detailed studies are needed to explore the effect of different geochemical factors on Mn^{2+} oxidation by ROS, such as ROS species, concentration, and pH, etc.

We also considered another possible pathway for Mn^{2+}(aq) oxidation, which is the comproportionation reaction on the surface of formed Mn(III,IV) oxides, Mn(II) + Mn(IV) → 2 Mn(III) (Elzinga, 2016). Both sides of the equation provide two electrons to react with LBB. On the left side, LBB reduces Mn(IV) to Mn(II) (2 electrons) and it does not react with Mn^{2+}(aq) (no electron transfer). On the right side of the equation, each Mn(III) has one electron transfer with LBB (total 2 electrons). Thus, after comproportionation-disproportionation, there should be no change in the amount of oxidized LBB. Therefore, the results indicate that the increase of Mn(III) equivalent, which is obtained from measuring the increase of oxidized LBB, results from the oxidation of Mn^{2+}(aq) to Mn(III) and Mn(III) to Mn(IV), not from comproportionation-dis proportionation. Thus, in our system, the dominant pathway for Mn^{2+}(aq) photo oxidation in the presence of goethite and hematite is the oxidation by holes in the valence band, resulting from the photoexcitation of an electron from the valence band to the conduction band. When goethite and hematite absorb energies greater than the band-gap, the generated holes at the valence band accept electrons from Mn^{2+}(aq). This reaction is thermodynamically feasible because the valence bands of goethite and hematite are at higher energy potentials than the reduction potential of Mn^{3+}(aq)/Mn^{2+}(aq) and MnO_2/Mn^{2+}(aq) (Fig. 3c). Such photocatalytic oxidation does not occur if there is no electron acceptor due to the recombination of the photo-excited electron and the hole. Indeed, under anoxic conditions, oxidation of Mn^{2+}(aq) was significantly suppressed, suggesting oxygen to be the acceptor of the photo-excited electron (Fig. 3d and e). In contrast, although the band gap of ferrihydrite (2.7 eV) is high enough to photocatalytically oxidize Mn^{2+}(aq), the absorbance spectrum of ferrihydrite shows poor photoexcitation (Fig. S9), which might have resulted in the insignificant photocatalytic oxidation of Mn^{2+}(aq).

4.2. Effect of solution chemistry in the photocatalytic oxidation of Mn^{2+}(aq) by Fe oxides

Solution chemistry can also affect the photooxidation process and products, as evidenced by the differences in DI vs ASW. The small pH difference in the DI-goethite (7.5 ± 0.1) vs ASW-goethite (7.9 ± 0.1) conditions likely did not induce significant differences in the oxidation rate (Fig. 1b and Fig. S4). High ionic strength (IS) and high concentrations of cations in ASW likely caused the observed differences in photooxidation kinetics/extent and products, as detailed below.

For the goethite system, the observed delay in oxidation for the first 3 h in ASW was likely due to the adsorption of cations on the goethite surface. Indeed, under dark conditions, the DI-goethite suspension showed minimal adsorption of Mn^{2+}(aq) on the goethite surface as indicated by a minimal change in Mn^{2+}(aq) concentration (Fig. S5b). In comparison, ASW-goethite suspension had ~10% Mn^{2+}(aq) adsorption on the goethite surface, and XPS results also indicated the adsorption of Na^+, Ca^{2+}, and Mg^{2+} on goethite in ASW (Fig. S10). These surface adsorbed cations possibly affected the arrangement of Mn atoms on the goethite surface. The nucleation and growth of groutite (1 × 2 tunnel structured Mn oxide) with similar lattice structure as goethite (1 × 2 tunnel structured Fe oxide) in DI-goethite suspension suggest that there was likely no significant disturbance to the arrangement of Mn oxides on the goethite surface in DI water. On the other hand, in ASW-goethite suspension, romanechite (with a different lattice structure from goethite) occurred on the goethite surface. Based on the phase difference of nucleated Mn oxides in ASW-goethite suspension, we can infer that surface impurities might affect the arrangement of Mn atoms on the goethite surface, and subsequently delay the nucleation event to form Mn oxide, as a critical number of Mn(III/IV) atoms need to be close to each other to overcome the supersaturation barrier and form a nucleus (De Yoreo and Vekilov, 2003).

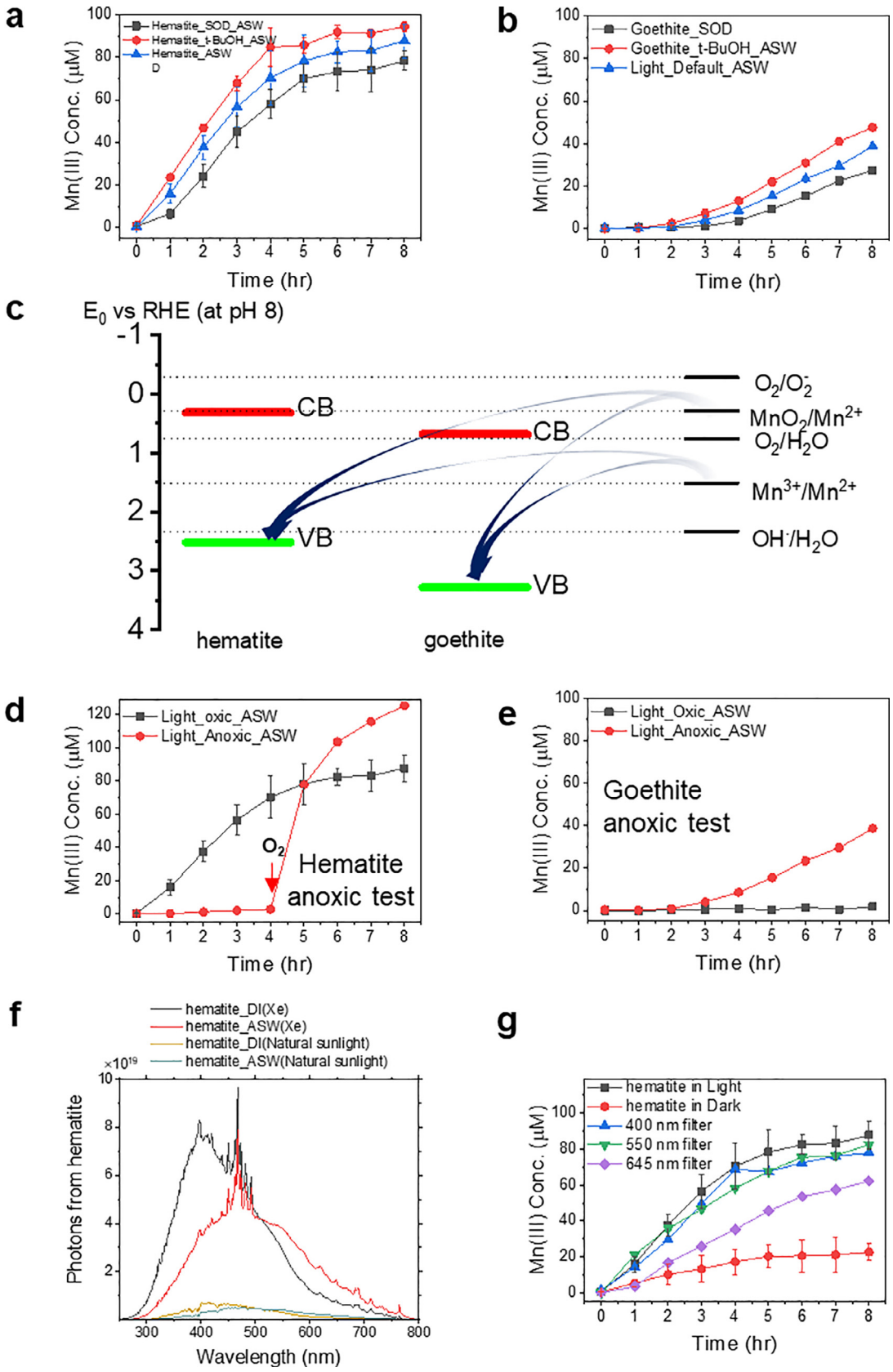
a
Hematite_SOD_ASW
Hematite_t-BuOH_ASW
Hematite_ASW
D
Mn(III) Conc. (μM)
Time (hr)
b
Goethite_SOD
Goethite_t-BuOH_ASW
Light_Default_ASW
Mn(III) Conc. (μM)
Time (hr)
c
E0 vs RHE (at pH 8)
CB
VB
CB
VB
O2/O2-
MnO2/Mn2+
O2/H2O
Mn3+/Mn2+
OH·/H2O
hematite
goethite
d
Light_oxic_ASW
Light_Anoxic_ASW
O2
Hematite
anoxic test
Mn(III) Conc. (μM)
Time (hr)
e
Light_Oxic_ASW
Light_Anoxic_ASW
Goethite
anoxic test
Mn(III) Conc. (μM)
Time (hr)
f
hematite_DI(Xe)
hematite_ASW(Xe)
hematite_DI(Natural sunlight)
hematite_ASW(Natural sunlight)
×10^19
Photons from hematite
Wavelength (nm)
g
hematite in Light
hematite in Dark
400 nm filter
550 nm filter
645 nm filter
Mn(III) Conc. (μM)
Time (hr)

For hematite system, although there was no delay of oxidation during the early stage of reaction, the oxidation rates are different under DI vs ASW conditions (Fig. 1). As shown in a previous study on the hydrothermal transformation of layer structured Mn oxides, the presence of large cations (e.g., Ca^{2+} and Mg^{2+}) can facilitate the formation of large tunnel structures (Feng et al., 2015), which is a possible explanation for the observed differences in DI-hematite and ASW-hematite suspensions. It also highlights the important roles of cations in the heterogeneous nucleation and growth of Mn oxides. While XRD and EXAFS analyses showed the nucleation of romanechite-like phase in ASW-goethite and hematite suspensions, clear phase identification of the Mn oxides on Fe oxide surface was challenging, due to the poorly crystalline nature of the Mn oxides and heterogeneity of the samples. Further detailed studies at atomic scale are warranted, such as high resolution transmission electron microscopy (HRTEM) and electron energy loss spectroscopy (EELS) analyses.

In addition, the optical absorbance spectra of hematite suspension were significantly different under DI vs ASW conditions (Fig. S11), likely due to the larger particle size of hematite in ASW driven by the strong IS in ASW. With increasing size of hematite nanoparticles, the lattice structure occurs with less tetrahedral and defective coordination of ferric ions (Chernyshova et al., 2010). In our system, the high IS of ASW likely affected the aggregation of hematite nanoparticles (Table S4) and subsequent light absorption spectra (Fig. S11). DI-hematite suspension shows a higher absorbance at wavelength below ~520 nm compared to that of ASW-hematite suspension. However, at wavelength above ~520 nm, ASW-hematite suspension shows higher absorbance. Using the absorbance spectra of hematite, calculations (details in *Supplementary Material* Text S1) showed higher photon absorption by hematite in DI (Fig. 3f). However, Mn^{2+}(aq) oxidation occurred at a slower rate and to a lesser extent in DI-hematite suspension as compared to ASW-hematite suspension (Fig. 1a). In the parallel experiments for the ASW-hematite system using 400, 550, and 645 nm cut-off optical filters, a considerable decrease in Mn^{2+}(aq) oxidation (from ~80 to ~60 μM at steady state) was only observed for the 645 nm filter (Fig. 3g). This suggests that electron transfer between hematite and Mn^{2+}(aq) occurs dominantly at ~650 nm (~1.9 eV). This light regime is known for the absorption band of ligand field transitions ($^6A_1 \rightarrow {}^4T_2({}^4G)$) of Fe^{3+} (Sherman and Waite, 1985; Sayed and Polshettiwar, 2015). Subsequently, these results suggest that Fe^{4+} holes generated from the transition are more photochemically active for Mn^{2+}(aq) oxidation than those generated by ligand to metal charge transfer, which occurs by a direct O^{2-} $2p^6 \rightarrow Fe^{3+}$ 3d transition ($\lambda < 400$ nm). Hematite showed more light absorption in ASW compared to DI for the transition of Fe^{3+} in octahedral environment (Fig. 3f and Fig. S11), and the results are consistent with the fast oxidation of Mn^{2+}(aq) with hematite in ASW than DI condition (Fig. 1a).

4.3. Implications for the formation of Mn oxides in natural systems

Our results suggest that mineral catalyzed photooxidation can be a significant yet previously overlooked pathway for the formation of tunnel structured Mn oxides in natural systems. By calculating quantum yields and extrapolating the Xe lamp intensity to natural sunlight (details in *Supplementary Material* Text S1), our results show that hematite and goethite catalyzed direct photocatalytic reactions can induce considerable oxidation of Mn^{2+}(aq) (Fig. 4a). It is worth noting that the calculation (0.1 g/L Fe oxides and 100 μM Mn^{2+} in ASW) is made conservatively considering the concentrations of Fe oxides (~60 to ~100 g/L) (Madison et al., 2013; Hermans et al., 2019) and Mn^{2+}(aq) (~50 to ~150 μM) (Madison et al., 2013)) at the surface of ocean sediments where the oxidation of dissolved Mn(II/III) dominantly occur in ocean systems. The calculated oxidation rates with natural sunlight are comparable to those of microbial processes (Francis and Tebo, 2001; Hansel and Francis, 2006; Learman et al., 2011a, 2011b; Toyoda and Tebo, 2013), which are generally considered as the dominant contributor for natural Mn^{2+}(aq) oxidation and Mn oxide formation. Note that all the oxidation rates in Fig. 4 (including those from this study and previous studies) are calculated using Mn(III) equivalent concentration. Due to the difference in experimental conditions between this study and previous biotic/abiotic processes, such as pH,

Fig. 3. Direct photocatalytic oxidation of Mn^{2+}(aq) by holes in a valence band of Fe oxides. (a and b) The photochemical reaction with hematite and goethite in ASW in the presence of ROS scavengers SOD and t-BuOH shows the insignificant effects of ROS on the oxidation of Mn^{2+}(aq). In the presence of SOD and t-BuOH, although different oxidation extents were observed in the first hour (likely due to different solution conditions such as cation adsorption on Fe oxides), the oxidation rates after 1 h were quite consistent. (c) The positions of band gaps and reduction potentials show that superoxide cannot be generated via photo-excited electrons from Fe oxides, and that the oxidation of Mn^{2+}(aq) occurs by the empty holes in the valence band. The positions of the valence bands were calculated at pH 8 (Li et al., 2018), and the positions of conduction band were consequently determined based on the band-gap energy of Fe oxides (2.2 and 2.6 eV for hematite and goethite, respectively (Gilbert, 2009; Zhang, 2011). (d) and (e) Anoxic experiments with hematite and goethite showing the important role of oxygen in the photocatalytic oxidation of Mn^{2+}(aq). Oxygen accepts photo-excited electrons from conduction band. For panel (d) dark anoxic experiment, the reactor lid was opened to air at 4 h, and the presence of oxygen immediately induced the oxidation of Mn^{2+}(aq). Because goethite ASW system showed overall slower oxidation than hematite, to clearly confirm the suppressed oxidation under anoxic condition, we maintained the anoxic condition for 8 h. (f) The calculated photons absorbed by hematite in DI water and ASW. By multiplying wavelength, constant for unit conversion, and absorbance of hematite or goethite, the photons absorbed by hematite or goethite in the exposure of Xe-lamp or natural sunlight can be calculated at each 1 nm width of wavelength. (g) Experiments conducted in the presence of 400, 550, or 645 nm cut-off optical filters.

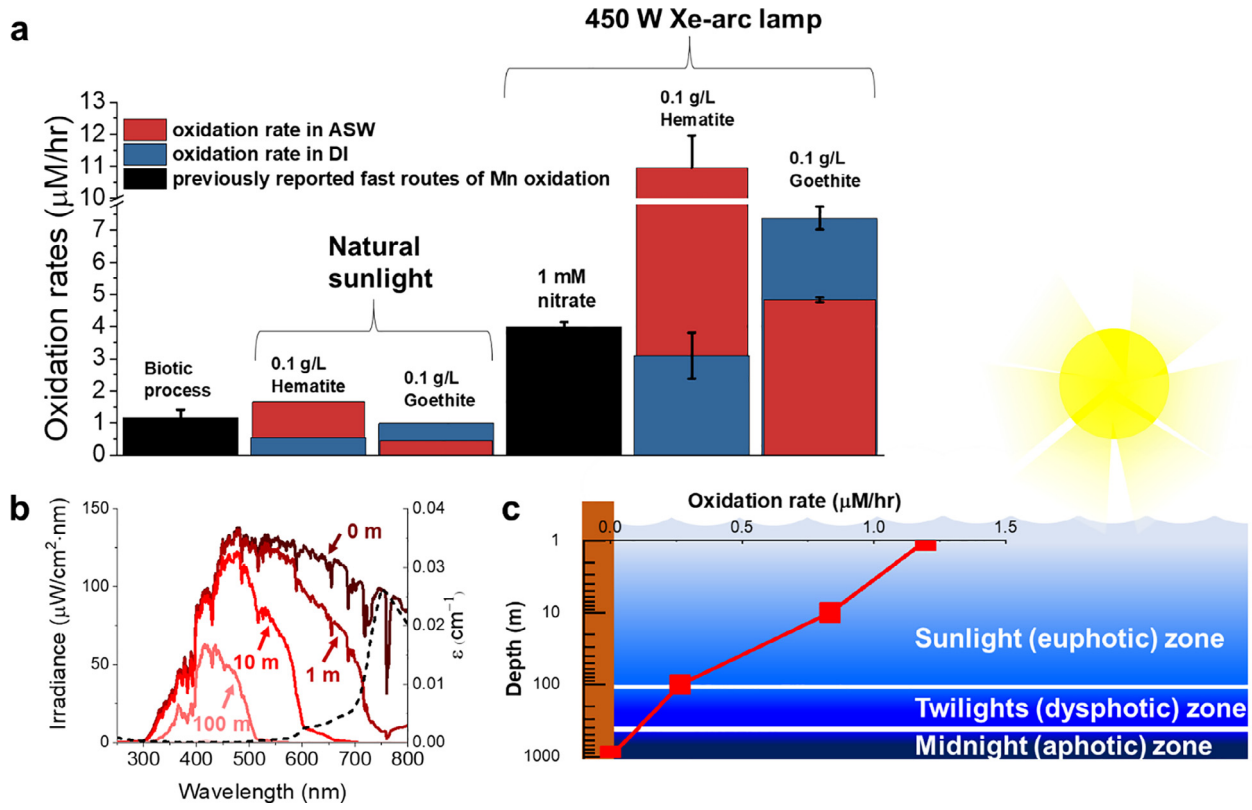

Fig. 4. Fast oxidation of Mn^{2+}(aq) by photocatalysis with Fe oxides in environmental systems. (a) Comparison of Mn^{2+}(aq) oxidation rates based on microbial processes, nitrate photolysis, and this work (Francis and Tebo, 2001; Hansel and Francis, 2006; Learman et al., 2011a; Learman et al., 2011b; Toyoda and Tebo, 2013; Jung et al., 2017a). The oxidation rates in the figure for both previous abiotic/biotic studies and this study are calculated from the consideration of Mn(III) equivalent. (b) Calculated irradiance of natural sunlight at varied water depths using extinction coefficient of water (Boivin et al., 1986; Pope and Fry, 1997) and irradiance of natural sunlight at surface. (c) Estimated oxidation rate of Mn^{2+}(aq) under hematite ASW condition, which showed the fastest oxidation rate among all the conditions, based on Fe oxide facilitated photochemical oxidation at varied water depths.

temperature, solution chemistry, etc., direct comparison of oxidation rates is limited. Nonetheless, this approximated comparison shows the potential importance of the photocatalytic oxidation by Fe oxides based on the rapid oxidation and abundance of Fe oxides in nature.

Further analysis shows that such photocatalytic oxidation processes can be also considerable at the surface of ocean sediments in euphotic zone (sun-lit aquatic environments, < ~200 m) (Fig. 4b and c). Using the extinction coefficient of water with the irradiance spectrum of natural sunlight (Boivin et al., 1986; Pope and Fry, 1997), we obtained a light spectrum as a function of the depth of water (Fig. 4b). Due to the relatively higher extinction coefficient at wavelengths higher than 600 nm, the irradiance decreases significantly with the depth of water. However, at ~100 m depth, ~22% of the sunlight at 250–600 nm, which is the greater part of visible and UV light, with equal or higher energy than the band-gaps of hematite and goethite to excite electrons from valence band to conduction band, can still penetrate the ocean (Fig. 4b). Although the changes in the light penetration spectrum can be affected by many factors, such as turbidity, phytoplankton, and dissolved organic matters, etc., the estimated oxidation of Mn^{2+}(aq) at various water depths shows that such Fe oxide facilitated photocatalytic oxidation of Mn^{2+}(aq) can occur in both terrestrial and shallow aquatic systems.

Overall, the explored photocatalytic abiotic pathway provides new insights on our current understanding of Mn oxide formation and the Mn redox cycle, as well as biogeochemical processes involving Mn oxides as a significant component. For example, it might provide new insights for understanding the commonly observed co-occurrence of Mn and Fe oxides in terrestrial and shallow aquatic systems, such as the layer-by-layer growth of Mn and Fe oxides in desert varnishes and ferromanganese nodules in lakes (Post, 1999; Lu et al., 2019). As compared to the fast oxidation of Fe(II) and formation of Fe oxides even under low oxygen conditions, the kinetics of Mn^{2+}(aq) oxidation is typically slow and the ubiquitous co-occurrence of Mn/Fe oxide is not well understood. This study demonstrates the feasibility of fast oxidation of Mn^{2+}(aq) and formation of Mn oxides on Fe oxides spanning terrestrial to ocean systems.

Our results also revealed the fast formation of tunnel structured Mn oxides (TMO) on Fe oxide surfaces. The formation of TMO via homogeneous oxidation under environ-

mental conditions has long puzzled the geoscience community (Feng et al., 2015), with significant knowledge gaps involving the sluggish reaction kinetics under low temperature circumneutral pH conditions, as well as the phase selection (e.g., tunnel size) (Jung et al., 2020). Our results not only revealed the fast formation of TMO under circumneutral environmental conditions, but also indicated the strong influences of mineral substrate and solution chemistry on the phase selection of Mn oxide products. In addition, during the heterogeneous nucleation of Mn oxides, impurities on natural Fe oxides can result in changes of the TMO tunnel size due to increased lattice mismatch at the interface between underlying Fe oxides and nucleating Mn oxides. Consequently, to reduce the structural lattice strains, the formation of a larger tunnel sized TMO, such as todorokite ($n \times 3$, with $n > 2$, the most common TMO in nature), might be more favorable on natural Fe oxides than smaller tunnel sized Mn oxides, such as romanechite and groutite, which are nucleated on the surface of pure Fe oxides in this study. Thus, the impact of mineral substrate, solution chemistry, and structural impurities might help explain the common presence of TMO with diverse structures in the natural environment (Post, 1999). Interestingly, different structures of natural Mn oxide coatings on Mn dendrites, desert varnish, stream deposits, etc. have been reported (Potter and Rossman, 1979), suggesting different nucleation and oxidation processes at work. With this in mind, one might consider using the structure of natural Mn oxides as a fingerprint for tracing the origin and environmental conditions during formation.

The observed direct photochemical oxidation of Mn^{2+}(aq) occurs via the electron transfer from Mn^{2+}(aq) to holes generated from the photoexcitation of electrons in Fe oxide minerals, not by the transfer between Mn^{2+}(aq) and oxygen related species (i.e., dissolved O_2 or ROS). For semiconductors, the photo-excited electrons will recombine with holes in the absence of electron acceptors. In this study, because oxygen is the only electron acceptor of the photo-excited electron, the oxidation of Mn^{2+}(aq) is suppressed under anoxic condition. However, in natural systems, natural organic/inorganic species with reduction potentials between the conduction band and valance band of Fe oxides can also accept the photo-excited electrons from Fe oxides. Given the long existence of organic molecules throughout Earth's history, our findings might provide possible explanations for the inference of the formation of Mn oxides prior to the significant rise of atmospheric oxygen level (Johnson et al., 2013; Planavsky et al., 2014a; Ossa Ossa et al., 2016). In the presence of natural electron acceptors, such photocatalytic oxidation of Mn^{2+}(aq) by Fe oxides, such as Banded Iron Formation (BIF) (Anbar and Holland, 1992; Kappler et al., 2005; Konhauser et al., 2017), might be feasible under minimal or low oxygen conditions that were previously thought to be too low for Mn(II) oxidation.

Declaration of Competing Interest

The authors declare that they have no known competing financial interests or personal relationships that could have appeared to influence the work reported in this paper.

ACKNOWLEDGEMENTS

This work is supported by U.S. National Science Foundation under Grant No. 1710285 (Y.T.). H.J. acknowledges the support by the National Research Foundation of Korea (NRF) (Grant No. 2021R1F1A1063426) and the Korea Ministry of Environment as Waste to Energy-Recycling Human Resource Development Project (Grant No. YL-WE-19-001). A.L acknowledges support by Natural Science Foundation of China (Grants No. 91851208 and 41820104003) and the DDE-IUGS Big Science Program. We thank beamline scientists at Beamlines 11-ID-B and 5-BM-D at Advanced Photon Source (APS), 4-1 at Stanford Synchrotron Radiation Lightsource (SSRL), and 6-BM at National Synchrotron Radiation Lightsource-II (NSLS-II). Use of APS, SSRL, and NSLS-II are supported by the US Department of Energy, Office of Science, Office of Basic Energy Sciences, under Contract No. DE-AC02-06CH11357, DE-AC02-76SF00515, and DE-SC0012704, respectively.

APPENDIX A. SUPPLEMENTARY MATERIAL

Supplementary data to this article can be found online at https://doi.org/10.1016/j.gca.2021.07.023.

REFERENCES

Anbar A. D. and Holland H. (1992) The photochemistry of manganese and the origin of banded iron formations. *Geochim. Cosmochim. Acta* **56**, 2595–2603.

Bargar J. R., Tebo B. M., Bergmann U., Webb S. M., Glatzel P., Chiu V. Q. and Villalobos M. (2005) Biotic and abiotic products of Mn (II) oxidation by spores of the marine *Bacillus* sp. strain SG-1. *Am. Mineral.* **90**, 143–154.

Boivin L.-P., Davidson W., Storey R., Sinclair D. and Earle E. (1986) Determination of the attenuation coefficients of visible and ultraviolet radiation in heavy water. *Appl. opt.* **25**, 877–882.

Butterfield C. N., Soldatova A. V., Lee S.-W., Spiro T. G. and Tebo B. M. (2013) Mn (II, III) oxidation and MnO_2 mineralization by an expressed bacterial multicopper oxidase. *Proc. Natl. Acad. Sci.* **110**, 11731–11735.

Cerrato J. M., Knocke W. R., Hochella M. F., Dietrich A. M., Jones A. and Cromer T. F. (2011) Application of XPS and solution chemistry analyses to investigate soluble manganese removal by MnOx(s)-coated media. *Environ. Sci. Technol.* **45**, 10068–10074.

Chaput D. L., Fowler A. J., Seo O., Duhn K., Hansel C. M. and Santelli C. M. (2019) Mn oxide formation by phototrophs: spatial and temporal patterns, with evidence of an enzymatic superoxide-mediated pathway. *Sci. Rep.* **9**, 18244.

Chernyshova I., Ponnurangam S. and Somasundaran P. (2010) On the origin of an unusual dependence of (bio) chemical reactivity of ferric hydroxides on nanoparticle size. *Phys. Chem. Chem. Phys.* **12**, 14045–14056.

Cornell R. M. and Schwertmann U. (2003) *The Iron Oxides: Structure, Properties, Reactions, Occurrences and Uses*. John Wiley & Sons.

Crowe S. A., Døssing L. N., Beukes N. J., Bau M., Kruger S. J., Frei R. and Canfield D. E. (2013) Atmospheric oxygenation three billion years ago. *Nature* **501**, 535–538.

Davies S. H. and Morgan J. J. (1989) Manganese (II) oxidation kinetics on metal oxide surfaces. *J. Colloid Interface Sci.* **129**, 63–77.

Daye M., Klepac-Ceraj V., Pajusalu M., Rowland S., Farrell-Sherman A., Beukes N., Tamura N., Fournier G. and Bosak T. (2019) Light-driven anaerobic microbial oxidation of manganese. *Nature* **576**, 311–314.

De Yoreo J. J., Gilbert P. U., Sommerdijk N. A., Penn R. L., Whitelam S., Joester D., Zhang H., Rimer J. D., Navrotsky A. and Banfield J. F. (2015) Crystallization by particle attachment in synthetic, biogenic, and geologic environments. *Science* **349**, aaa6760.

De Yoreo J. J. and Vekilov P. G. (2003) Principles of crystal nucleation and growth. *Rev. Mineral. Geochem.* **54**, 57–93.

Diem D. and Stumm W. (1984) Is dissolved Mn^{2+} being oxidized by O_2 in absence of Mn-bacteria or surface catalysts? *Geochim. Cosmochim. Acta* **48**, 1571–1573.

Elzinga E. J. (2011) Reductive transformation of birnessite by aqueous Mn(II). *Environ. Sci. Technol.* **45**, 6366–6372.

Elzinga E. J. (2016) 54Mn radiotracers demonstrate continuous dissolution and reprecipitation of vernadite (δ-MnO_2) during interaction with aqueous Mn(II). *Environ. Sci. Technol.* **50**, 8670–8677.

Fendorf S. E. and Zasoski R. J. (1992) Chromium(III) oxidation by delta-MnO_2. 1. Characterization. *Environ. Sci. Technol.* **26**, 79–85.

Feng X., Zhao H., Liu F., Cui H., Tan W. and Li W. (2015) *Transformation from Phyllomanganates to Todorokite under Various Conditions: A Review of Implication for Formation Pathway of Natural Todorokite, Advances in the Environmental Biogeochemistry of Manganese Oxides*. American Chemical Society, pp. 107–134.

Feng X. H., Tan W. F., Liu F., Wang J. B. and Ruan H. D. (2004) Synthesis of todorokite at atmospheric pressure. *Chem. Mater.* **16**, 4330–4336.

Feng X. H., Zhu M., Ginder-Vogel M., Ni C., Parikh S. J. and Sparks D. L. (2010) Formation of nano-crystalline todorokite from biogenic Mn oxides. *Geochim. Cosmochim. Acta* **74**, 3232–3245.

Francis C. A. and Tebo B. M. (2001) Enzymatic manganese (II) oxidation by a marine α-proteobacterium. *Appl. Environ. Microbiol.* **67**, 4024–4029.

Frei R., Gaucher C., Poulton S. W. and Canfield D. E. (2009) Fluctuations in Precambrian atmospheric oxygenation recorded by chromium isotopes. *Nature* **461**, 250–253.

Gilbert Benjami et al. (2009) Band-gap measurements of bulk and nanoscale hematite by soft x-ray spectroscopy. *Phys. Rev. B* **79** (3), 035108.

Goto K. T., Sekine Y., Shimoda G., Hein J. R., Aoki S., Ishikawa A., Suzuki K., Gordon G. W. and Anbar A. D. (2020) A framework for understanding Mo isotope records of Archean and Paleoproterozoic Fe- and Mn-rich sedimentary rocks: Insights from modern marine hydrothermal Fe-Mn oxides. *Geochim. Cosmochim. Acta* **280**, 221–236.

Hansel C. M. and Francis C. A. (2006) Coupled photochemical and enzymatic Mn (II) oxidation pathways of a planktonic Roseobacter-like bacterium. *Appl. Environ. Microbiol.* **72**, 3543–3549.

Hansel C. M., Zeiner C. A., Santelli C. M. and Webb S. M. (2012) Mn (II) oxidation by an ascomycete fungus is linked to superoxide production during asexual reproduction. *Proc. Natl. Acad. Sci.* **109**, 12621–12625.

Hermans M., Lenstra W. K., Hidalgo-Martinez S., van Helmond N. A. G. M., Witbaard R., Meysman F. J. R., Gonzalez S. and Slomp C. P. (2019) Abundance and Biogeochemical Impact of Cable Bacteria in Baltic Sea Sediments. *Environ. Sci. Technol.* **53**, 7494–7503.

Ilton E. S., Post J. E., Heaney P. J., Ling F. T. and Kerisit S. N. (2016) XPS determination of Mn oxidation states in Mn (Hydr) oxides. *Appl. Surf. Sci.* **366**, 475–485.

Johnson J. E., Webb S. M., Thomas K., Ono S., Kirschvink J. L. and Fischer W. W. (2013) Manganese-oxidizing photosynthesis before the rise of cyanobacteria. *Proc. Natl. Acad. Sci.* **110**, 11238–11243.

Jung H., Chadha T., Kim D., Biswas P. and Jun Y.-S. (2017a) Photochemically-assisted fast abiotic oxidation of manganese and formation of δ–MnO_2 nanosheets in nitrate solution. *Chem. Commun.* **53**, 4445–4448.

Jung H., Chadha T. S., Min Y., Biswas P. and Jun Y.-S. (2017b) Photochemically-assisted synthesis of birnessite nanosheets and their structural alteration in the presence of pyrophosphate. *ACS Sustain. Chem. Eng.* **5**, 10624–10632.

Jung H., Taillefert M., Sun J., Wang Q., Borkiewicz O. J., Liu P., Yang L., Chen S., Chen H. and Tang Y. (2020) Redox cycling driven transformation of layered manganese oxides to tunnel structures. *J. Am. Chem. Soc.* **142**, 2506–2513.

Kappler A., Pasquero C., Konhauser K. O. and Newman D. K. (2005) Deposition of banded iron formations by anoxygenic phototrophic Fe(II)-oxidizing bacteria. *Geology* **33**, 865–868.

Konhauser K., Planavsky N., Hardisty D., Robbins L., Warchola T., Haugaard R., Lalonde S., Partin C., Oonk P. and Tsikos H. J. E.-S. R. (2017) Iron formations: a global record of Neoarchaean to Palaeoproterozoic environmental history. *Earth-Sci. Rev.* **172**, 140–177.

Lanza N. L., Fischer W. W., Wiens R. C., Grotzinger J., Ollila A. M., Cousin A., Anderson R. B., Clark B. C., Gellert R., Mangold N., Maurice S., Le Mouélic S., Nachon M., Schmidt M., Berger J., Clegg S. M., Forni O., Hardgrove C., Melikechi N., Newsom H. E. and Sautter V. (2014) High manganese concentrations in rocks at Gale crater. *Mars. Geophys. Res. Lett.* **41**, 5755–5763.

Learman D., Voelker B., Vazquez-Rodriguez A. and Hansel C. (2011a) Formation of manganese oxides by bacterially generated superoxide. *Nat. Geosci.* **4**, 95–98.

Learman D., Wankel S., Webb S., Martinez N., Madden A. and Hansel C. (2011b) Coupled biotic–abiotic Mn (II) oxidation pathway mediates the formation and structural evolution of biogenic Mn oxides. *Geochim. Cosmochim. Acta* **75**, 6048–6063.

Li Y., Xu X., Li Y., Ding C., Wu J., Lu A., Ding H., Qin S. and Wang C. (2018) Absolute band structure determination on naturally occurring rutile with complex chemistry: Implications for mineral photocatalysis on both Earth and Mars. *Appl. Surf. Sci.* **439**, 660–671.

Lu A., Li Y., Ding H., Xu X., Li Y., Ren G., Liang J., Liu Y., Hong H., Chen N., Chu S., Liu F., Li Y., Wang H., Ding C., Wang C., Lai Y., Liu J., Dick J., Liu K. and Hochella M. F. (2019) Photoelectric conversion on Earth's surface via widespread Fe- and Mn-mineral coatings. *Proc Natl. Acad. Sci.*, 201902473.

Luther, III, G. W. (2010) The role of one-and two-electron transfer reactions in forming thermodynamically unstable intermediates as barriers in multi-electron redox reactions. *Aquat. Geochem.* **16**, 395–420.

Madden A. S. and Hochella M. F. (2005) A test of geochemical reactivity as a function of mineral size: manganese oxidation promoted by hematite nanoparticles. *Geochim. Cosmochim. Acta* **69**, 389–398.

Madison A. S., Tebo B. M. and Luther G. W. (2011) Simultaneous determination of soluble manganese(III), manganese(II) and total manganese in natural (pore)waters. *Talanta* **84**, 374–381.

Madison A. S., Tebo B. M., Mucci A., Sundby B. and Luther G. W. (2013) Abundant porewater Mn (III) is a major component of the sedimentary redox system. *Science* **341**, 875–878.

Manceau A., Marcus M. A. and Grangeon S. (2012) Determination of Mn valence states in mixed-valent manganates by XANES spectroscopy. *Am. Mineral.* **97**, 816–827.

McKeown D. A. and Post J. E. (2001) Characterization of manganese oxide mineralogy in rock varnish and dendrites using X-ray absorption spectroscopy. *Am. Mineral.* **86**, 701–713.

Millero F. J. (2016) *Chemical Oceanography*. CRC Press.

Montserrat F., Renforth P., Hartmann J., Leermakers M., Knops P. and Meysman F. J. R. (2017) Olivine dissolution in seawater: implications for CO_2 sequestration through enhanced weathering in coastal environments. *Environ. Sci. Technol.* **51**, 3960–3972.

Mulholland P. J. (1997) Dissolved organic matter concentration and flux in streams. *J. North Am. Benthol. Soc.* **16**, 131–141.

Murray K. J., Webb S. M., Bargar J. R. and Tebo B. M. (2007) Indirect oxidation of Co(II) in the presence of the marine Mn (II)-oxidizing bacterium *Bacillus* sp strain SG-1. *Appl. Environ. Microbiol.* **73**, 6905–6909.

Nealson K. H. and Saffarini D. (1994) Iron and manganese in anaerobic respiration – environmental significance, physiology, and regulation. *Annu. Rev. Microbiol.* **48**, 311–343.

Nico P. S., Anastasio C. and Zasoski R. J. (2002) Rapid photo-oxidation of Mn (II) mediated by humic substances. *Geochim. Cosmochim. Acta* **66**, 4047–4056.

Ossa Ossa F., Hofmann A., Vidal O., Kramers J. D., Belyanin G. and Cavalazzi B. (2016) Unusual manganese enrichment in the Mesoarchean Mozaan Group, Pongola Supergroup, South Africa. *Precambrian Res.* **281**, 414–433.

Owens J. D., Nielsen S. G., Horner T. J., Ostrander C. M. and Peterson L. C. (2017) Thallium-isotopic compositions of euxinic sediments as a proxy for global manganese-oxide burial. *Geochim. Cosmochim. Acta* **213**, 291–307.

Planavsky N. J., Asael D., Hofmann A., Reinhard C. T., Lalonde S. V., Knudsen A., Wang X., Ossa Ossa F., Pecoits E., Smith A. J. B., Beukes N. J., Bekker A., Johnson T. M., Konhauser K. O., Lyons T. W. and Rouxel O. J. (2014a) Evidence for oxygenic photosynthesis half a billion years before the Great Oxidation Event. *Nat. Geosci.* **7**, 283–286.

Planavsky N. J., Reinhard C. T., Wang X., Thomson D., McGoldrick P., Rainbird R. H., Johnson T., Fischer W. W. and Lyons T. W. (2014b) Low Mid-Proterozoic atmospheric oxygen levels and the delayed rise of animals. *Science* **346**, 635–638.

Pope R. M. and Fry E. S. (1997) Absorption spectrum (380–700 nm) of pure water. II. Integrating cavity measurements. *Appl. Opt.* **36**, 8710–8723.

Post J. E. (1999) Manganese oxide minerals: crystal structures and economic and environmental significance. *Proc. Natl. Acad. Sci.* **96**, 3447–3454.

Potter R. M. and Rossman G. R. (1979) Mineralogy of manganese dendrites and coatings. *Am. Mineral.* **64**, 1219–1226.

Ravel B. and Newville M. (2005) ATHENA, ARTEMIS, HEPHAESTUS: data analysis for X-ray absorption spectroscopy using IFEFFIT. *J. Synchrotron Radiat.* **12**, 537–541.

Santelli C. M., Webb S. M., Dohnalkova A. C. and Hansel C. M. (2011) Diversity of Mn oxides produced by Mn (II)-oxidizing fungi. *Geochim. Cosmochim. Acta* **75**, 2762–2776.

Saratovsky I., Gurr S. J. and Hayward M. A. (2009) The structure of manganese oxide formed by the fungus *Acremonium* sp. strain KR21-2. *Geochim. Cosmochim. Acta* **73**, 3291–3300.

Sayed F. N. and Polshettiwar V. (2015) Facile and sustainable synthesis of shaped iron oxide nanoparticles: effect of iron precursor salts on the shapes of iron oxides. *Sci. Rep.* **5**, 9733.

Sherman D. M. and Waite T. D. (1985) Electronic spectra of Fe3+ oxides and oxide hydroxides in the near IR to near UV. *Am. Mineral.* **70**, 1262–1269.

Soldatova A. V., Balakrishnan G., Oyerinde O. F., Romano C. A., Tebo B. M. and Spiro T. G. (2019) Biogenic and synthetic MnO_2 nanoparticles: size and growth probed with absorption and Raman spectroscopies and dynamic light scattering. *Environ. Sci. Technol.* **53**, 4185–4197.

Stone A. T. and Morgan J. J. (1984) Reduction and dissolution of manganese(III) and manganese(IV) oxides by organics. 1. Reaction with hydroquinone. *Environ. Sci. Technol.* **18**, 450–456.

Sunda W. G. and Kieber D. J. (1994) Oxidation of humic substrances by manganese oxides yields low-molecular-weight organic substrates. *Nature* **367**, 62–64.

Sung W. and Morgan J. J. (1981) Oxidative removal of Mn (II) from solution catalysed by the γ-FeOOH (lepidocrocite) surface. *Geochim. Cosmochim. Acta* **45**, 2377–2383.

Tebo B. M., Clement B. G. and Dick G. J. (2007) Biotransformations of manganese. *Manual Environ. Microbiol.* **3**, 1223–1238.

Toyoda K. and Tebo B. M. (2013) The effect of Ca^{2+} ions and ionic strength on Mn (II) oxidation by spores of the marine *Bacillus* sp. SG-1. *Geochim. Cosmochim. Acta* **101**, 1–11.

van Genuchten C. M. and Peña J. (2017) Mn(II) oxidation in Fenton and Fenton type systems: identification of reaction efficiency and reaction products. *Environ. Sci. Technol.* **51**, 2982–2991.

Webb S., Fuller C., Tebo B. and Bargar J. (2006) Determination of uranyl incorporation into biogenic manganese oxides using X-ray absorption spectroscopy and scattering. *Environ. Sci. Technol.* **40**, 771–777.

Webb S., Tebo B. and Bargar J. (2005a) Structural characterization of biogenic Mn oxides produced in seawater by the marine Bacillus sp. strain SG-1. *Am. Mineral.* **90**, 1342–1357.

Webb S. M. (2005) SIXPack a graphical user interface for XAS analysis using IFEFFIT. *Phys. Scr.* **T115**, 1011–1014.

Webb S. M., Dick G. J., Bargar J. R. and Tebo B. M. (2005b) Evidence for the presence of Mn (III) intermediates in the bacterial oxidation of Mn (II). *Proc. Natl. Acad. Sci.* **102**, 5558–5563.

Wehrli B., Friedl G. and Manceau A. (1995) Reaction rates and products of manganese oxidation at the sediment-water interface. In *Aquatic Chemistry: Interfacial and Interspecies Processes* (eds. C. P. Huang, C. R. Omelia and J. J. Morgan). American Chemical Society, pp. 111–134.

World Health, O (2003) *Nitrate and nitrite in drinking-water: background document for development of WHO guidelines for drinking-water quality*. World Health Organization, Geneva.

Wu J., Cheng S., Cai M.-H., Wu Y.-P., Li Y., Wu J.-C., Li A.-M. and Li W.-T. (2018) Applying UV absorbance and fluorescence indices to estimate inactivation of bacteria and formation of bromate during ozonation of water and wastewater effluent. *Water Res.* **145**, 354–364.

Wu W., Changzhong J. and Roy V. A. L. (2015) Recent progress in magnetic iron oxide–semiconductor composite nanomaterials as promising photocatalysts. *Nanoscale* **7**, 38–58.

Xu X., Li Y., Li Y., Lu A., Qiao R., Liu K., Ding H. and Wang C. (2019) Characteristics of desert varnish from nanometer to micrometer scale: a photo-oxidation model on its formation. *Chem. Geol.* **522**, 55–70.

Xu Y. and Schoonen M. A. J. A. M. (2000) The absolute energy positions of conduction and valence bands of selected semiconducting minerals. *Am. Mineral.* **85**, 543–556.

Yang P., Lee S., Post J. E., Xu H., Wang Q., Xu W. and Zhu M. (2018) Trivalent manganese on vacancies triggers rapid transformation of layered to tunneled manganese oxides (TMOs): implications for occurrence of TMOs in low-temperature environment. *Geochim. Cosmochim. Acta* **240**, 173–190.

Yang P., Wen K., Beyer K. A., Xu W., Wang Q., Ma D., Wu J. and Zhu M. (2021) Inhibition of oxyanions on redox-driven transformation of layered manganese oxides. *Environ. Sci. Technol.* **55**, 3419–3429.

Zhang Hengzhon et al. (2011) Size-Dependent Bandgap of Nanogoethite. *J. Phys. Chem. C* **115**(36), 17704–17710.

Associate editor: Mario Villalobos